Published by IOP Publishing for Sissa Medialab

Received: *June 28, 2017*
Accepted: *August 10, 2017*
Published: *September 6, 2017*

Measurements of the spatial magnetic field distribution in a z-pinch plasma throughout the stagnation process

G. Rosenzweig,[1,2] E. Kroupp, A. Fisher and Y. Maron

Faculty of Physics, Weizmann Institute of Science,
234 Herzl St., Rehovot 7610001, Israel

E-mail: tzvitzvi@gmail.com

Abstract: We report on measurements, made for the first time for an imploding plasma at its stagnation, of the magnetic field spatial distribution. Utilized for the measurements is a spectroscopic technique based on simultaneous recording of each of the left- and right-handed circularly polarized Zeeman emissions. While this method allows for overcoming the Stark- and Doppler-broadenings that obscure the Zeeman splitting, it requires a line of sight that is parallel to the magnetic field lines. To this end, the radial charge-state distribution in the stagnating z-pinch plasma was measured, and the method was employed for emission lines of several selected charge states located in various radial locations. This also allowed for measuring the time-resolved magnetic field radial distribution in a single discharge, which is advantageous for high-energy-density plasma experiments. These distributions were measured at various locations along the pinch axis.

Keywords: Plasma diagnostics - charged-particle spectroscopy; Plasma diagnostics - high speed photography; Plasma diagnostics - interferometry, spectroscopy and imaging

[1]Corresponding author.
[2]Present address: Plasma Science and Fusion Center, Massachusetts Institute of Technology, Cambridge, MA 02139, U.S.A.

https://doi.org/10.1088/1748-0221/12/09/P09004

2017 JINST 12 P09004

Contents

2017 JINST 12 P09004

1 Introduction

Knowledge of the magnetic field distribution in a z-pinch plasma is of high importance since the plasma-field interaction plays a key role in determining the characteristics of the stagnation process and the efficiency of the energy coupling to the plasma. Various theoretical models and simulation schemes of z-pinch plasmas strongly rely on the magnetic field distribution for predictions of the hydrodynamic and atomic processes in the plasma [1, 2].

Plasma conditions that are typical of high-energy-density (HED) systems often render the common Zeeman-splitting magnetic-field-diagnostic impossible. The high densities and high ion velocities result in broad spectral line-shapes that smear out the Zeeman-split patterns, even when polarization techniques are employed to remove the π-Zeeman components from the spectrum [3]. Moreover, when the magnetic field magnitude and direction vary in time over the measurement temporal resolution scale, or over spatial scales that are below the diagnostic system resolution (here denoted as "non-directional field"), polarization techniques are either inapplicable or provide ambiguous results. The present work deals with fields of a preferred direction, where polarization techniques are useful.

In general, spectroscopic methods based on the Zeeman effect for the determination of magnetic fields in plasmas, are limited due to their sensitivity to density- or temperature-induced broadenings [4, 5]. Alternative approaches to Zeeman spectroscopy are based on Farady rotation [6–9], $\dot{B}$ probes [10–13] or proton beam deflectometry [14–18]. Yet each of the methods has its own difficulties. The rotation of the plane of polarization of an electromagnetic wave passing though a plasma is proportional to $\int n_e \cdot B \cdot \mathrm{d}l$, where n_e is the electron density [8]. Therefore, Faraday rotation requires knowledge of electron densities at all locations where the magnetic field information is to be extracted, adding another source of error. In addition, reconstructing the magnetic field requires Abel inversion, which assumes cylindrical symmetry. Electrical probe diagnostics are intrusive and provide limited spatial resolution that is determined by geometric constraints set by the probe size and the experimental complexities. Proton beam deflectometry, while capable of measuring both the electric and the magnetic fields separately [15], requires either a short-pulse high-intensity laser or a fusion reaction for the beam generation. Furthermore, it necessitates 3D simulations of the fields and of the proton trajectories to interpret the experimental results. Thus, Expanding the usefulness of non-intrusive spectroscopic tools based on the Zeeman effect to HED conditions is desirable.

While Zeeman splitting has been used to measure magnetic fields in imploding plasma experiments [3, 19–23], as yet the effect was mainly used to measure the field in z-pinches at a single radial position. For gaining insight into the hydrodynamic processes in HED plasmas, it is essential to obtain experimentally the magnetic field spatial distribution, rather than determine the field magnitude in a limited region. To the best of our knowledge, in z-pinch investigations, thus far the Zeeman effect was used to measure this distribution only in ref. [3], where the measurements were limited to relatively far from the stagnating plasma ($r > 7$ mm) and to times earlier than 90 ns before stagnation on axis.

Here we report on measurements of $B(r)$ before, during, and after stagnation and at radial locations much closer to the stagnating plasma than in ref. [3]. We used the method, denoted here by "the two-polarizations method", that is described in refs. [19, 21, 24, 25] and provides the highest sensitivity to the field magnitude of all the Zeeman-based methods, as explained below. This method was applied in a z-pinch experiment in ref. [21], where it was employed for the edge of the plasma column. Indeed, an important advantage in the present work is obtaining the field spatial distribution for various times during the implosion and stagnation. This was achieved by taking advantage of naturally-formed plasma conditions gradients, without the need for Abel inversion techniques that assume symmetry and require very good signal-to-noise ratios.

2 Diagnostic methods

2.1 The two-polarizations method

When the perturbation in the energy levels due to the magnetic field is small compared to the fine-structure energy separations, the magnetic-field-induced splitting for both the upper and the lower levels of the transition is given by

$$\Delta E = g_{LSJ}\mu_B M B, \tag{2.1}$$

where B is the magnitude of the magnetic field $\vec{B}$, M is the projection of the total angular momentum J of the given state in the direction of $\vec{B}$, μ_B is the Bohr magneton, and g_{LSJ} is the Landé g factor [26]. Of the transitions between the split levels, only those for which $\Delta M = 0$ (π components), $+1$ (σ^+ components) or -1 (σ^- components) are allowed.

If a dominant direction of $\vec{B}$ exists, the emissions from the components of a Zeeman split transition are polarized, depending on the viewing angle relative to $\vec{B}$. When the emission is viewed parallel to $\vec{B}$, only the σ components are observable and the light is circularly polarized, right handed for σ^+ and left handed for σ^-. Emission viewed perpendicular to $\vec{B}$ is linearly polarized, with the π and σ components polarized parallel and perpendicular to $\vec{B}$, respectively. When viewed at intermediate angles with respect to $\vec{B}$ the light is elliptically polarized (ref. [27], pp. 835-840).

The only known spectroscopic approach for a reliable determination of non-directional fields is based on the comparison of line shapes of different fine-structure components of the same multiplet [26, 28]. This method utilizes the fact that these components undergo different Zeeman splittings in a magnetic field, while the other line-broadening mechanisms, namely the Stark and the Doppler effects and the instrumental broadening, are practically identical for the two components. Therefore, if these two multiplet components can be recorded simultaneously, the difference between the line shapes, that (in the absence of opacity) is only due to B, can be used to determine the field.

Two different methods, based on the emission polarization properties, are applicable when a dominant direction of $\vec{B}$ exists. In the first technique, useful for lines of sight that are approximately perpendicular to $\vec{B}$, the field is determined by detecting the relative contributions of the π and σ Zeeman components to the observed line shape. Using this method, the time-dependent radial distribution of B in a high density CO_2 gas-puff z-pinch plasma implosion has been determined [3], allowing for concluding that during the implosion the plasma conducts the entire circuit current. By comparing the data to the solution of the magnetic diffusion equation, the electrical conductivity of the plasma was determined and found to be in agreement with the Spitzer value. However, since it was required that the curvature of $\vec{B}$ along the azimuthal dimension within the observed plasma region be negligible, the measurements were limited to large radii and early times, as mentioned above.

In the two methods described, B is obtained from comparison between line widths. This limits the minimum field magnitude measurable and requires high-accuracy line shape measurements and a high signal-to-noise ratio [5]. The third method, also applicable only when a dominant direction of $\vec{B}$ exists, is based on independently recording the full line shapes of the left- and right-handed circularly polarized components of Zeeman-split emissions observed along multiple chords through the plasma [21]. Discriminating between the σ^+ and σ^- components is achieved using a quarter-wave plate and a linear polarizer. The quarter-wave plate transforms the circular polarizations into orthogonal linear polarizations, at $\pm 45°$ to its extraordinary axis. Placing a linear polarizer at one of these angles allows only one of the polarizations to pass. While the σ^+ components are always blue-shifted with respect to the unpolarized emission line, the σ^- components are always red-shifted. This method therefore provides the highest sensitivity to B, and is nearly unaffected by opacity since it relies on the line positions rather than on their shapes.

2.2 Use of various charge states to obtain radial dependence using the chordal observations

A key requirement of the third method described, is that the lines of sight must be parallel to $\vec{B}$. Considering the cylindrical geometry of a z-pinch, this requirement can only be fulfilled by viewing the plasma side-on and focusing on the very edge of the cylinder. At first sight, this seems to yield a single data point per experiment that provides B at the outermost radius of the plasma column. Assuming azimuthal symmetry, the integrated current obtained from this result via Apmère's law (see eq. (5.1)) is the entire current flowing within this radius. This provides the total current flowing through the plasma, but gives no indication of the magnetic field distribution or of the current density.

As said above, a crucial need is obtaining the spatial distribution of the magnetic field in the plasma throughout the pinch process, and particularly during the final stages of the implosion and

2017 JINST 12 P09004

stagnation. This was achieved in this work by simultaneously measuring the Zeeman effect of spectral lines emitted from different charge states that are located at different radial positions.

In z-pinches designed to produce a high K-emission yield during the 10-ns-long stagnation phase, generally $\sim$ 15% of the imploding plasma is heated at stagnation to conditions necessary to radiate K emission, at both low- and high-current experiments [1, 29]. In the final stages of implosion and during stagnation, a considerable temperature gradient exists, from the hot and dense core towards the colder peripheral plasma. This generates a radial charge-state distribution, from highly charged ions found at the core, to lower charge states that reside at outer layers (as illustrated in figure 2).

For each charge state, the emission line most useful for the observation of the Zeeman effect is selected. Then, this line is observed chordally at the outermost radius for which a satisfactory signal is achieved, which yields a view nearly parallel to the magnetic field lines at that radius, within a small radial spread. Measuring lines from several charge states simultaneously provides the magnetic field magnitude at several radii, yielding the field radial distribution in a single experiment. Assuming azimuthal symmetry, each such data point yields the total current flowing within its radius, producing a current profile from which the current density can be derived.

3 Experimental setup

A gas-puff system, consisting of a fast electromagnetic valve and a double nozzle (annular opening with a central hole), is used to produce an on-axis jet, $\sim$ 5 mm in diameter, surrounded by a cylinder shell, $\sim$ 38 mm in diameter, inside the main vacuum chamber. A cylindrical anode is positioned inside the chamber, co-axially with the nozzle (cathode), at a variable distance, set to 9 mm. A high-voltage discharge circuit, powered by a 60-kV, 5.5-μF capacitor bank, produces a peak current of 500 kA, rising in $\sim$ 500 ns (measured using a calibrated $\dot{B}$ probe). The operating gas throughout the present experiments is O_2, and is ionized with high-energy electrons prior to the current initiation. The implosion time is designed to match the current rise time, and the stagnation phase, characterized by x-ray emission, lasts $\sim$ 10 ns.

To obtain reliably the spectral separation between the σ^+ and σ^- components, both polarizations must be measured simultaneously. This is achieved by using a polarizing beam-splitter cube that splits the radiation passing through the quarter-wave plate into two beams, each carrying one of the two orthogonal linear polarizations. Each of those beams is transmitted via a branch of a bifurcated optical fibers bundle to form a single bundle, the image of which is projected onto the slit of a spectrometer (see figure 1). Each branch is composed of a row of fifty 200-μm-core fibers. Emission from the z-pinch plasma is imaged onto the array through the quarter-wave plate and the beam splitter. Each of the fibers of a given branch views a chord at a different distance from the pinch axis. The plasma is imaged onto the fibers with a 1 : 1 ratio, so that the spatial resolution is 250 μm (including the 50-μm spacing between adjacent fibers). This resolution is usually reduced to 1 mm by integrating over four fibers, to improve the signal-to-noise ratio. Both branches are aligned so that they view the exact same spatial region within the plasma, and are subsequently merged to form a single line of 100 fibers.

Each branch of the fiber array is oriented perpendicular to the pinch axis (the z-axis), such that the fibers view several chords through the plasma, at a common axial position (see figure 2). The

2017 JINST 12 P09004

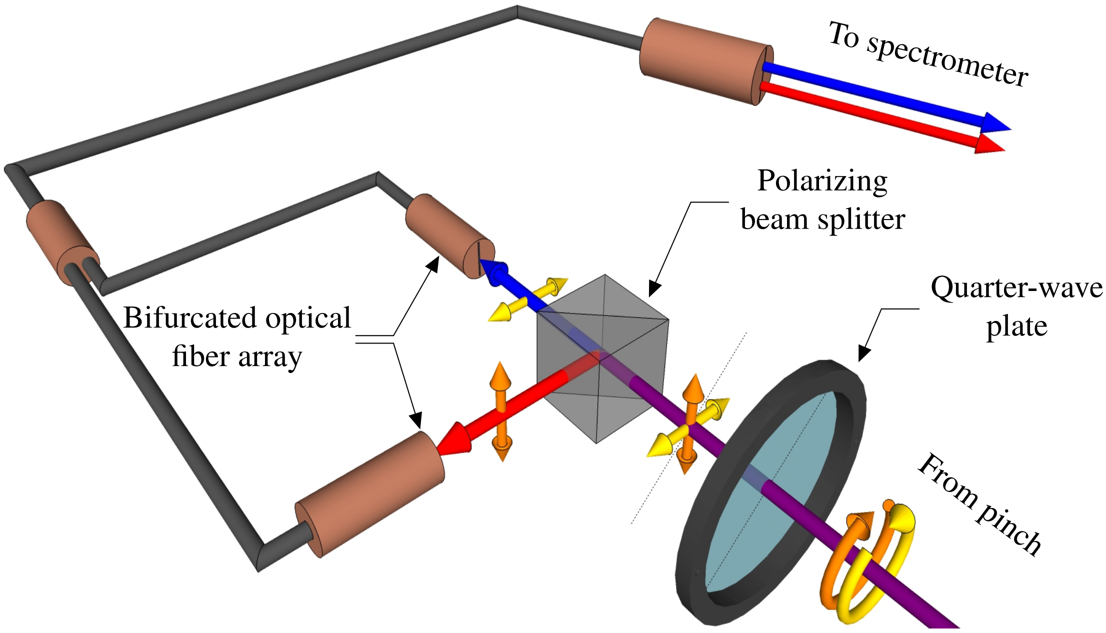

Figure 1. Polarization-spectroscopy setup. The circular polarizations of the emission from the z-pinch plasma are transformed by a quarter-wave plate into orthogonal linear polarizations. Each polarization is then directed by a polarizing beam splitter to a different branch of a bifurcated optical fiber array. The joint end of the array is imaged into a spectrometer that records the spectra from different locations, for each polarization, at a single discharge.

joint end of the array is imaged onto the entrance slit of a 1.26 m SPEX spectrometer, equipped with a 2400 $\frac{\text{grooves}}{\text{mm}}$ grating. An intensified charge-coupled-device (ICCD) camera is coupled to the exit focal plane of the spectrometer. The ICCD is equipped with a cooled CCD of 1024 × 1024-pixels (each 13 × 13 μm^2 in area). One image is taken per discharge with the ICCD gated at 10 ns. The spectroscopic system has a good sensitivity between 2000 and 7000 Å. The polarization optics (the quarter-wave plate and the polarizing beam splitter cube) were chosen to suit the spectral lines of interest: the O VI 3811.35-Å line and the O III 3791.26-Å line, as described below.

An additional ICCD (1024 × 256-pixels, each 15 × 15 μm^2 in area) is operated concurrently with the spectrometer ICCD, to record 2D side-on UV-visible-light images of the plasma. Neutral density filters and a 380 nm bandpass filter were alternately used. Since a considerable fraction of the visible light is continuum radiation, using the different filters showed no significant difference in the plasma structure. These images, such as in figure 3, grant a better understanding of the spectrograms obtained, and provide the outermost radius of the plasma column, used to calculate the boundary magnetic field, as explained below.

4 Data analysis

4.1 Determination of the magnetic field from the shifted polarizations

The spectrogram shown in figure 4 was taken with a 10-ns exposure centered at $t = -16$ ns, where $t = 0$ is the time of peak x-ray yield during stagnation. The fibers were positioned to view the

2017 JINST 12 P09004

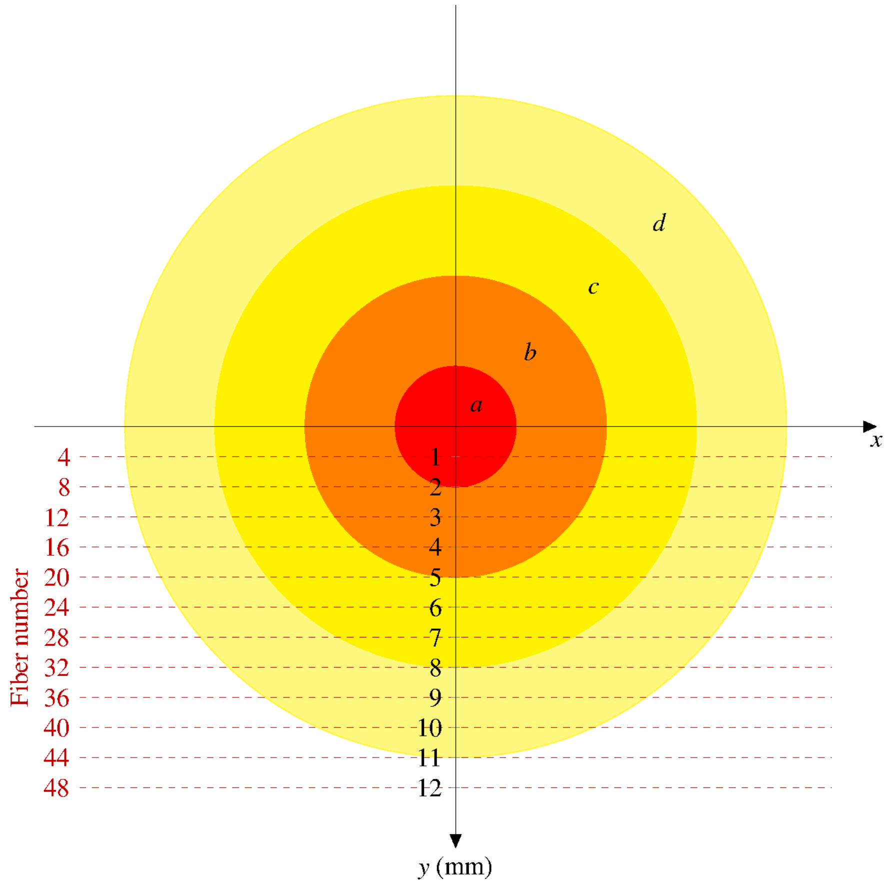

Figure 2. Schematic top view of a layered plasma column and the chordal views. As an example, four layers are described, each containing different charge states. Twelve lines of sights, out of the 50 provided by the fiber array, are displayed, with their ordinal number in the array given in red. These lines of sight are parallel to the x-axis and are spaced along the y-axis (chordal positions). Lines of sight closer to $y = 0$ mm collect contributions from more charge states. Only the lines of sight tangent to the outer edges of the different layers, such as $y = 2, 5, 8,$ and 11 mm, can provide reliably the magnetic field magnitude.

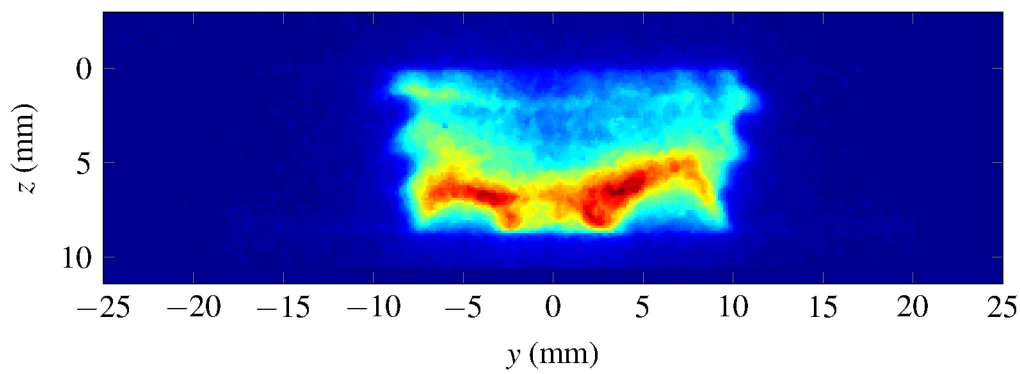

Figure 3. 2D image taken simultaneously with the spectrogram in figure 4.

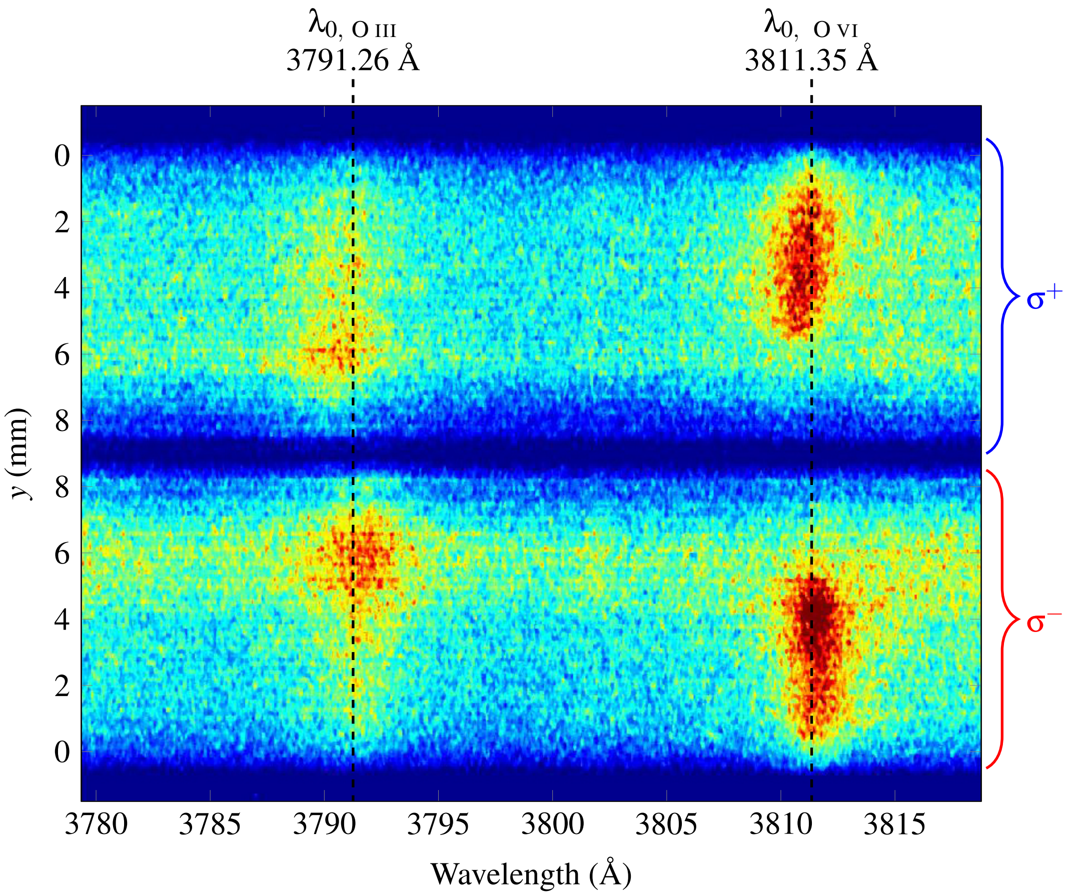

Figure 4. Spectrogram taken at $z = 5$ mm ± 0.5 mm with a 10-ns exposure centered at $t = -16$ ns. The upper and lower halves show the spectra at various chordal positions for the σ^+ and σ^- polarizations, respectively, with each polarization collected by a different branch of the optical fiber array. At the entrance to the spectrometer, the two fiber bundles, each of 50 fibers, are arranged along a straight line (a single linear array) that is imaged along the spectrometer input slit. They are so arranged that those viewing the pinch center ($y = 0$ mm) are at the array upper and lower edges, and the chordal positions of the lines of sight increase towards the linear array center (as recorded by the camera image shown in this figure). The dashed lines depict the unshifted wavelengths of the O III and O VI spectral lines.

plasma at $z = 5$ mm ± 0.5 mm, where $z = 0$ mm is the cathode edge and $z = 9$ mm is the anode edge. It is evident that while the σ^+ lines (top half) are blue-shifted relative to the unshifted wavelengths, λ_0, the σ^- lines are red-shifted. Each of the horizontal lineouts is a spectrum obtained from a single fiber and is therefore emitted from a known chordal position (y-coordinate). Due to vignetting, comparing spectra to each other is more accurate if those spectra are at a similar distance from the center of the ICCD screen. Therefore, the linear fiber arrays (branches) for the two orthogonal polarizations were aligned so that at the input of the spectrometer, the fibers looking at the pinch axis are farthest from the array center for both branches, as shown in figure 4.

DC calibration lamps were used to ascertain that no spectral shift is present in the absence of a magnetic field. Furthermore, the spectral separation between the polarizations was seen to change

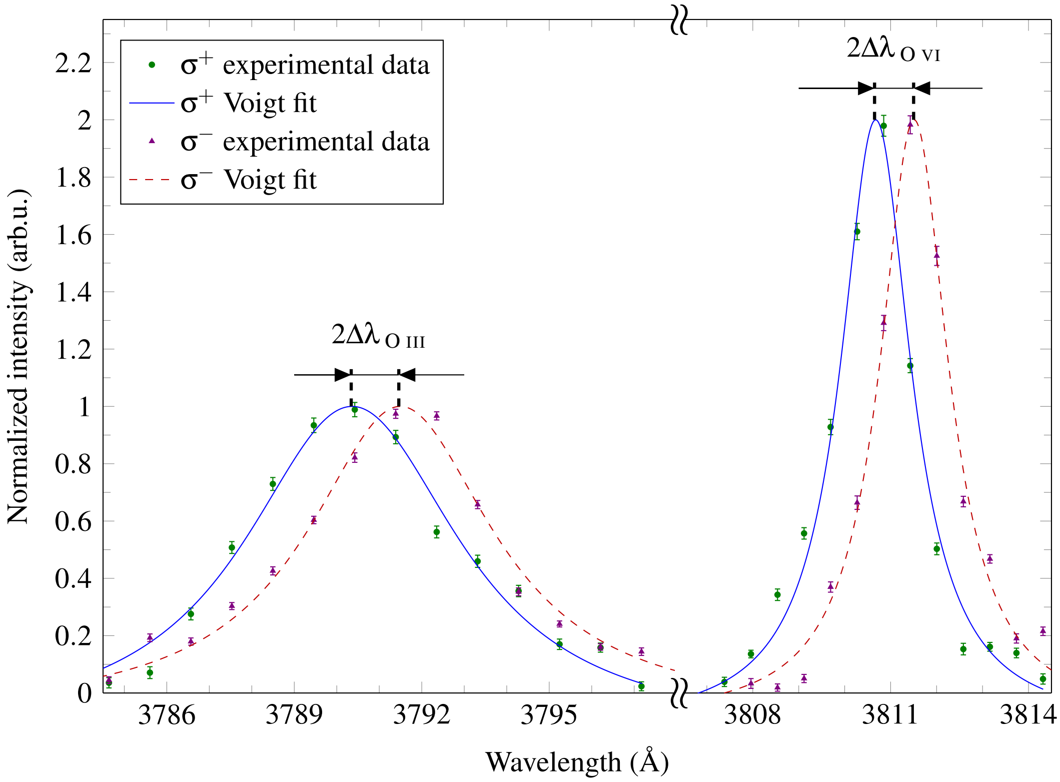

Figure 5. Analysis of the (a) O III 3791.26-Å and of the (b) O VI 3811.35-Å lines seen in figure 4. The measured line shapes of each of the σ polarizations are fit with Voigt profiles, from which the Zeeman effect is obtained. The separation between the polarized-line positions is twice the wavelength shift, $\Delta\lambda$, calculated using eq. (2.1).

for measurements taken at different times due to a different degree of field penetration. At early times, when the field is predominately at the plasma periphery, no shift was seen for a line of the inner charge state (O VI).

The emission lines observed in the present work are isolated, resulting in Lorentzian Stark broadening shapes. The other contribution to the line shapes broadening is the Doppler broadening that results from the ion thermal motion and the spread of their hydrovelocities in the direction of observation. The line shapes recorded are also affected by the instrumental spectral response, where this contribution and that of the Doppler broadening are nearly Gaussian. Therefore, inferring the magnetic field magnitude from a measured line requires fitting a Voigt profile to each polarization line shape, from which the wavelength of its peak is obtained (figure 5). The spectral separation between the peaks of the σ^+ and the σ^- profiles of each line is then compared with a Zeeman splitting calculation based on eq. (2.1).

It is worth noting that when a single transition with $\Delta M = +1$ and a single one with $\Delta M = -1$ exist (such as for ${}^2S_{\frac{1}{2}} - {}^2P_{\frac{1}{2}}$), their peak-positions are unaffected by the broadening mechanisms. Thus, the peak-positions of the shifted components are readily determined. However, when there are two or more components per σ polarization (as for ${}^2S_{\frac{1}{2}} - {}^2P_{\frac{3}{2}}$), they may overlap due to the Stark and Doppler broadenings and form a single line profile. The peak-position for each polarization then depends on the relative contributions of its components, and can therefore be affected by individual-component broadening. In the data analysis, in order to obtain the correct values of the spectral shifts, the entire structure, resulting from all components and their shapes, was calculated. To this end, we used various emission lines to obtain the Doppler broadening and to obtain the electron density, either from Stark broadening or from line intensity ratios, as described in refs. [30–32]. Calculations for the spectral lines measured in this research, using a wide range of parameters typical of our plasma, proved that this effect is almost negligible; incorporating it into the error analysis contributed a little to the error bars.

4.2 Sources of errors

Performing imaging of the plasma onto the optical fibers gives rise to three sources of errors. Light is both collected and refracted by the lens within acceptance cones, determined by the optical properties of the various elements and by the geometry of the system (the vacuum chamber, ports and distances). Therefore, both the lens and the fibers accept light from a spread of angles.

All optical elements up to the fibers are placed along a common optical axis, viewing the plasma parallel to $\vec{B}$ at the outer layer radii, as explained above. Emissions along this line exhibit circular polarizations of the σ components and have no contribution from the π components. However, due to the optics' acceptance angles mentioned above, emissions are also collected from other azimuths, thus observing emission from regions where $\vec{B}$ is not parallel to the line of sight. For this emission the σ components are elliptically polarized, and there is a finite projection of the π components on the lens plane, leading to spectral content in each branch of the fiber array that is not solely from the expected σ polarization.

Another source of "leakage" of polarizations from one branch to the other is the variation of the quarter-wave plate retardance with the direction of the propagation in the crystal. This variation is because both the optical path length and the refractive index for the extraordinary component vary with the direction of propagation [33]. Therefore, circularly polarized light incident on the waveplate at an angle of incidence larger than zero, will not be completely linearly polarized uppon exiting the crystal.

The third error source originates at the dependence of the diattenuation (polarizing efficiency) of the polarizing beam splitter cube on the angle of incidence, as measured from the normal to the beam splitting interface. The beam splitter is optimized for light incident upon this interface at 45°. Two reasons for a decrease in the diattenuation are: (1) the s- and p-component orientations (which define the polarizing axes) at the beam-splitting interface vary with the direction of propagation, and (2) the performance of the beam splitting interface is a function of the angle of incidence [34]. The transmittance curves of the s and p components are blue-shifted for increasing incidence angles and red-shifted for decreasing angles. The effect is more severe for decreasing angles, as the transmittance for p-polarized light drops rapidly for even small deviations [35]. Since the transmittance curve of the p polarization determines the lower bound of the beam splitter bandwidth, shorter wavelengths are affected more seriously.

Mitigation of these effects can be achieved, when there is sufficient light, by placing an iris near the lens, thus contracting the base of the cones and therefore reducing the maximum angle of incidence. Another way to lessen the latter two sources of error, which are more severe than the first, is to construct a telecentric telescope by placing additional lenses to collimate the light

2017 JINST 12 P09004

before it reaches the waveplate, and to re-focus it between the beam splitter and the fibers. This, however, makes the apparatus quite cumbersome and complicates the alignment procedure for different wavelengths. Furthermore, the angle of incidence of the collimated light will only be ideal for a point source placed on the optical axis. Owing to the fact that the goal is to record emissions from several radii simultaneously, resulting in an extended source, light will be incident at several angles even if a telecentric telescope is used. These angles can be reduced by performing imaging with a ratio other than 1 : 1, at the expense of the spatial resolution.

It is noteworthy that all three mechanisms cause the splitting to become *smaller* than it would be in their absence, thus making the derived magnitude of the magnetic field be a lower bound for its true value. As described in the following section, the combined uncertainty from all these effects was demonstrated to be smaller than 5% for our system, and was therefore incorporated in the upper error bar.

In order to determine the angular dependence of the polarization optics, a mock-up of the experimental setup was constructed. Circularly polarized white-light was imaged onto the optical fibers through the polarization optics. Since the entire beam was polarized with the same handedness, one branch of the fiber array would remain completely dark, had the beam remained collimated. The leakage of light to this branch was calculated as a percentage of the light reaching the other branch, taking into account the relative transmittance of all fibers.

As expected, it was found that leakage from the p- to the s-polarization is more significant than contrariwise. In addition, shorter wavelengths exhibited stronger leakage. The results were then used in our simulation code.

Estimating the effect of collecting light within the acceptance cone was done by calculating, for every line of sight not parallel to $\vec{B}$, the polarizations of all π and σ components and the contributions of all components to the spectra of the otherwise pure σ^+ or σ^- components. This calculation also included the cylindrical geometry of the pinch, as well as integrating over all angles within the acceptance cone.

5 Results and discussion

As mentioned above, the two spectral lines used in this work are the O vi 3811.35-Å line and the O iii 3791.26-Å line. These lines are in a spectral proximity, so that they can be simultaneously observed by the spectrometer, yet they are isolated from each other and from neighboring lines for the plasma parameters typical of our experiments. The charges of O vi and O iii are sufficiently different so that they reside in distinctively different radii. Abel inversion is performed for the intensity of each line, obtained from the various fibers, to extract the outermost radius of each charge-state layer.

An additional data point, the boundary magnetic field, B_0, is obtained for each discharge via Apmère's law, assuming the entire circuit current, I_0, measured by the $\dot{B}$ probe outside the pinch region, flows within the plasma cylinder in the pinch [3]. This current is assumed to flow within the outermost plasma radius R_0, extracted from the 2D plasma images discussed above. B_0 is thus obtained via

$$B_0 = \frac{\mu_B I_0}{2\pi R_0}. \tag{5.1}$$

The magnetic field distributions for two time instants are given in figure 6. A detailed analysis and a discussion of these and other results are being prepared for publication.

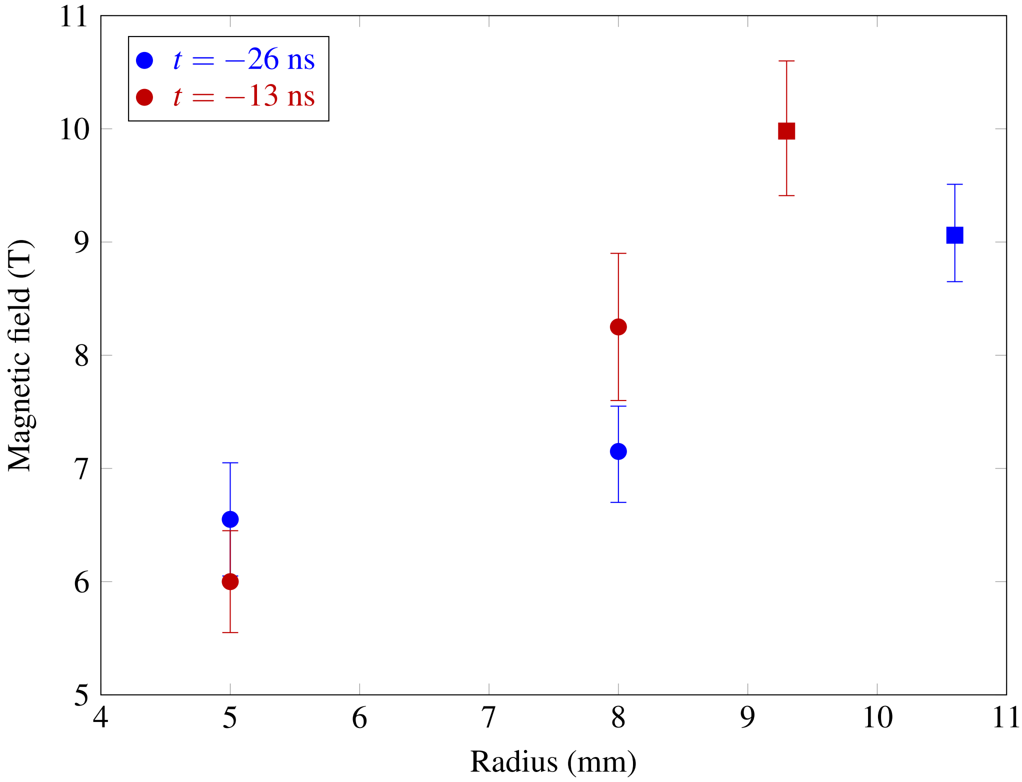

Figure 6. Magnetic field distribution at two moments in time prior to stagnation, with z = 5 mm ± 0.5 mm. The circles represent values obtained from the O vi (innermost radii) and the O iii spectral lines, and the squares represent the boundary magnetic field, B_0, obtained from I_0.

6 Conclusions

A method for measuring the magnetic field distribution in a z-pinch plasma during the final stages of the implosion and the stagnation was developed. The field magnitude at several radii is obtained in a single discharge, by incorporating measurements of the charge-state distribution with polarization spectroscopy. The latter is used to discriminate between the two circularly polarized σ polarizations of Zeeman split emission lines, when viewed parallel to $\vec{B}$.

Evidently, in this work, dopant-ions can be introduced to allow for a broader selection of transitions at the various radial locations, and to expand the determination of $B(r)$ to smaller radii.

Acknowledgments

This research is supported in part by the Israel Science Foundation, the NSF-BSF foundation and AFSOR. The authors are grateful to J. L. Giuliani, A. L. Velikovich and R. Doron for helpful discussions and for reading the manuscript.

References

[1] D.D. Ryutov, M.S. Derzon and M.K. Matzen, *The physics of fast z pinches*, *Rev. Mod. Phys.* **72** (2000) 167.

[2] J.L. Giuliani and R.J. Commisso, *A review of the gas-puff z-pinch as an X-ray and neutron source*, *IEEE Trans. Plasma Sci.* **43** (2015) 2385.

[3] G. Davara, L. Gregorian, E. Kroupp and Y. Maron, *Spectroscopic determination of the magnetic-field distribution in an imploding plasma*, *Phys. Plasmas* **5** (1998) 1068.

[4] G.A. Rochau, J.E. Bailey and Y. Maron, *Applied spectroscopy in pulsed power plasmas*, *Phys. Plasmas* **17** (2010) 055501.

[5] R. Doron et al., *Determination of magnetic fields based on the Zeeman effect in regimes inaccessible by Zeeman-splitting spectroscopy*, *High Energy Density Phys.* **10** (2014) 56.

[6] J.A. Stamper and B.H. Ripin, *Faraday-rotation measurements of megagauss magnetic fields in laser-produced plasmas*, *Phys. Rev. Lett.* **34** (1975) 138.

[7] M. Borghesi, A.J. MacKinnon, A.R. Bell, R. Gaillard and O. Willi, *Megagauss magnetic field generation and plasma jet formation on solid targets irradiated by an ultraintense picosecond laser pulse*, *Phys. Rev. Lett.* **81** (1998) 112.

[8] S.N. Bland et al., *Use of Faraday probing to estimate current distribution in wire array z pinches*, *Rev. Sci. Instrum.* **77** (2006) 10E315.

[9] V.V. Ivanov, A.A. Anderson, D. Papp, A.L. Astanovitskiy, V. Nalajala and O. Dmitriev, *Study of magnetic fields and current in the z pinch at stagnation*, *Phys. Plasmas* **22** (2015) 092710.

[10] G.G. Zukakishvili et al., *Measurements of the azimuthal magnetic field within imploding multiwire arrays in the Angara-*5-1 *facility*, *Plasma Phys. Rept.* **31** (2005) 908.

[11] J. Greenly, M. Martin, I. Blesener, D. Chalenski, P. Knapp and R. McBride, *The role of flux advection in the development of the ablation streams and precursors of wire array z-pinches*, *AIP Conf. Proc.* **1088** (2009) 53.

[12] P.F. Knapp et al., *Growth and saturation of the axial instability in low wire number wire array z pinches*, *Phys. Plasmas* **17** (2010) 012704.

[13] P.-A. Gourdain et al., *Initial magnetic field compression studies using gas-puff z-pinches and thin liners on COBRA*, *Nucl. Fusion* **53** (2013) 083006.

[14] M. Borghesi et al., *Proton imaging: a diagnostic for inertial confinement fusion/fast ignitor studies*, *Plasma Phys. Control. Fusion* **43** (2001) A267.

[15] C.K. Li et al., *Measuring E and B fields in laser-produced plasmas with monoenergetic proton radiography*, *Phys. Rev. Lett.* **97** (2006) 135003.

[16] P.M. Nilson et al., *Magnetic reconnection and plasma dynamics in two-beam laser-solid interactions*, *Phys. Rev. Lett.* **97** (2006) 255001.

[17] N.L. Kugland, D.D. Ryutov, C. Plechaty, J.S. Ross and H.-S. Park, *Invited article: relation between electric and magnetic field structures and their proton-beam images*, *Rev. Sci. Instrum.* **83** (2012) 101301.

[18] D. Mariscal et al., *Measurement of pulsed-power-driven magnetic fields via proton deflectometry*, *Appl. Phys. Lett.* **105** (2014) 224103.

2017 JINST 12 P09004

[19] F.C. Jahoda, F.L. Ribe and G.A. Sawyer, *Zeeman-effect magnetic field measurement of a high-temperature plasma*, Phys. Rev. **131** (1963) 24.

[20] N.J. Peacock and B.A. Norton, *Measurement of megagauss magnetic fields in a plasma focus device*, Phys. Rev. **A 11** (1975) 2142.

[21] R.P. Golingo, U. Shumlak and D.J.D. Hartog, *Note: Zeeman splitting measurements in a high-temperature plasma*, Rev. Sci. Instrum. **81** (2010) 126104.

[22] M.R. Gomez et al., *Magnetic field measurements via visible spectroscopy on the Z machine*, Rev. Sci. Instrum. **85** (2014) 11E609.

[23] J.T. Banasek, J.T. Engelbrecht, S.A. Pikuz, T.A. Shelkovenko and D.A. Hammer, *Measuring* 20–100 *T B-fields using Zeeman splitting of sodium emission lines on a* 500 *kA pulsed power machine*, Rev. Sci. Instrum. **87** (2016) 11D407.

[24] J.F. Seely, U. Feldman, N.R. Sheeley Jr., S. Suckewer and A.M. Title, *Magnetic field measurements based on the Zeeman splitting of forbidden transitions*, Rev. Sci. Instrum. **56** (1985) 855.

[25] T. Shikama and P.M. Bellan, *Development of a polarization resolved spectroscopic diagnostic for measurements of the vector magnetic field in the Caltech coaxial magnetized plasma jet experiment*, Rev. Sci. Instrum. **84** (2013) 023507.

[26] E. Stambulchik, K. Tsigutkin and Y. Maron, *Spectroscopic method for measuring plasma magnetic fields having arbitrary distribution of direction and amplitude*, Phys. Rev. Lett. **98** (2007) 225001.

[27] C. Cohen-Tannoudji, B. Diu, F. Laloe and B. Dui, *Quantum mechanics (*2 *volume set)*, Wiley-Interscience, U.S.A., October 2006.

[28] S. Tessarin et al., *Beyond Zeeman spectroscopy: magnetic-field diagnostics with stark-dominated line shapes*, Phys. Plasmas **18** (2011) 093301.

[29] E. Kroupp et al., *Ion temperature and hydrodynamic-energy measurements in a z-pinch plasma at stagnation*, Phys. Rev. Lett. **107** (2011) 105001.

[30] L. Gregorian, V. Bernshtam, E. Kroupp, G. Davara and Y. Maron, *Use of emission-line intensities for a self-consistent determination of the particle densities in a transient plasma*, Phys. Rev. **E 67** (2003) 016404.

[31] L. Gregorian et al., *Electron density and ionization dynamics in an imploding z-pinch plasma*, Phys. Plasmas **12** (2005) 092704.

[32] L. Gregorian et al., *Electron-temperature and energy-flow history in an imploding plasma*, Phys. Rev. **E 71** (2005) 056402.

[33] P.D. Hale and G.W. Day, *Stability of birefringent linear retarders (waveplates)*, Appl. Opt. **27** (1988) 5146.

[34] J.L. Pezzaniti and R.A. Chipman, *Angular dependence of polarizing beam-splitter cubes*, Appl. Opt. **33** (1994) 1916.

[35] Bernhard Halle Nachfolger GmbH, G. Zinner, private communication, (2014).

2017 JINST 12 P09004